2023 IEEE International Conference on Robotics and Automation (ICRA 2023)
May 29 - June 2, 2023. London, UK

# Robotic Method and Instrument to Efficiently Synthesize Faulty Conditions and Mass-Produce Faulty-Conditioned Data for Rotary Machines

Yip Fun Yeung[1], Fangzhou Xia[1], Juliana Covarrubias[1], Mikio Furokawa[2],Takayuki Hirano[2] and Kamal Youcef-Toumi[1]

***Abstract*— Condition synthesis is vital for generating data for fault detection and diagnosis studies. Traditional methods rely heavily on human labor. This study proposes a robotic method and its instrument to efficiently synthesize faulty conditions and mass-produce data to develop fault detection and diagnosis algorithms. The first contribution is the formalization of a new approach called Robotic Condition Synthesis, which shifts the traditionally labor-intensive task of condition synthesis to a robot-based force control task. The second contribution is developing a new robotic manipulator, which is more effective than current lab-grade robots for the tasks involved in the Robotic Condition Synthesis. The third contribution is empirical evidence of the superiority of this new robot in performing the Robotic Condition Synthesis tasks. This study also explores the potential of the new robot by conducting a three-dimensional system identification of a rotordynamic plant, which lays the foundation for more advanced Robotic Condition Synthesis policies in the future.**

**Keywords: Sustainable Production and Service Automation; Failure Detection and Recovery; Engineering for Robotic Systems**

## I. Introduction and Background

One of the significant challenges to developing new algorithms on fault detection and diagnosis (FDD) is the limited availability of high-quality data [1–5]. To overcome this shortage, some researchers generate their own data by synthesizing various healthy and faulty operating conditions of a target plant through a process known as condition synthesis (CS). However, state-of-the-art CS methods, which often rely on manual enumeration of heuristically defined sets of faulty configurations, can lead to low-quality data. This is a significant bottleneck in FDD research, as noted in [6].

This study introduces a new approach to generate data for fault detection and diagnosis research called Robotic Condition Synthesis (R−CS). This method replaces traditional manual methods with a robotic approach to modulate the dynamics of a target plant, actively imitating healthy or faulty working conditions. The R−CS process involves two interrelated topics: (a) Designing control policies that mimic the dynamics of various working conditions and (b) Planning tasks, modeling contacts, and designing the robot to execute the control policies effectively. This study focuses on the latter topic while briefly discussing essential aspects of the former.

Common laboratory-grade robots are not well-suited for the task of Robotic Condition Synthesis. Two robot force control policies are designed for R−CS in this study to simulate the behavior of various faulty conditions in a rotordynamic plant. These policies require the robot to deliver precise force trajectories with high bandwidth and repeatability while having an extensive workspace, a large payload capacity, and minimal mechanical nonlinearities. However, these conflicting requirements are challenging for lab-grade robots across a wide range of performance [7–10] to fulfill. This gap in suitable and generalizable robots for the R−CS tasks inspire the development of a novel **Ca**rtesian **M**ulti-**A**ctuation **R**obot (**CaMAR**).

This research has three key contributions to the field: (a) The formalization of a novel method, referred to as Robotic Condition Synthesis, which is derived from a model-based framework. The R−CS method represents a significant departure from traditional condition synthesis methods, as it shifts from manual operation to a robotic paradigm, thereby enhancing the efficiency of the dataset generation process. (b) The design and development of a novel robotic manipulator, CaMAR, which has been specifically engineered to meet the unique functional requirements of R−CS tasks. (c) The utilization of the CaMAR to perform an automated multi-dimensional dynamical system identification on a benchtop rotordynamic plant demonstrates the effectiveness of the robot and lays the foundation for further optimization of the R−CS control policies in future studies.

The paper is organized as follows: we review state-of-the-art (SOTA) CS practices in Sec.II. Sec.III formalizes the R−CS method from a model-based perspective and proposes a comprehensive R−CS pipeline. In Sec.IV, we propose the design methodology of the CaMAR. Finally, experiments and validation of the CaMAR to effectively conduct R−CS tasks are demonstrated in Sec.V.

## II. State of the Art Manual Condition Synthesis

In a typical condition synthesis procedure, as first described in [11], there are three conceptual roles involved: an operator, an antagonist, and a data acquisition agent (DAQ). The operator operates a target plant with the desired input; the antagonist injects various types of preset faults into the plant in a controlled manner, and the DAQ objectively measures the plant's operation. For example, in a sensor system, an antagonist can synthesize sensor drifting, biasing, and circuit shortage faults [11,12]; the synthetic faults of a rotordynamic plant often consist of axes misalignment, unbalanced load, bent shaft, bearing faults and rub-impact [13–20]. The antagonist artificially injects faults and records them. These recorded faults are further cast into *labels*, and compiled with the *feature* signals captured by the DAQ into a dataset. The dataset is subsequently utilized to develop FDD algorithms.

Condition syntheses in past literature rely heavily on manual practices. A typical manual condition synthesis (M−CS) is demonstrated in Fig.1. Consider a conceptual *condition space* $\mathbb{C}$ containing all possible healthy/faulty conditions of interest. The M−CS first prescribes a loosely-defined subset of conditions $\mathbb{C}_\epsilon \subset \mathbb{C}$, e.g., millimeter-scale through-holes with four diameters on four different locations of two types of bearings in the Case Western Reserve University (CWRU) bearing-fault dataset [20], a major benchmark in the FDD research community. For every synthetic runtime $i$, the M−CS samples a condition instance $c_{\epsilon,i} \in \mathbb{C}_\epsilon$ and install it on a baseline rotordynamic plant. The operator

*This work is supported by The Japan Steel Works, LTD., Japan

[1] Department of Mechanical Engineering, Massachusetts Institute of Technology, Cambridge, MA, 02139, USA.
[3] The Japan Steel Works, LTD., Hiroshima Plant, Japan.

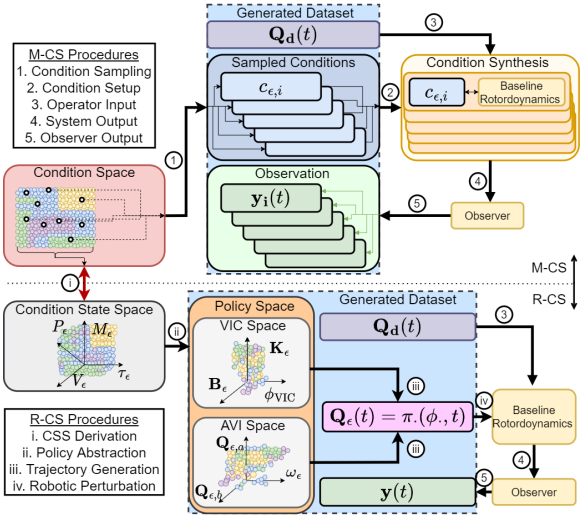


Fig. 1. The SOTA M-CS and proposed R-CS pipelines.

commands a desired input $\mathbf{Q_{d,i}}(t)$ to the plant, and the output of the system is observed $\mathbf{y_i}(t)$ by a state observer. Assuming $\mathbf{Q_{d,i}}(t)$ is fully-observable, the two time-series sequences are combined as $\boldsymbol{\mathcal{X}}_i(t) \triangleq \big(\mathbf{Q_{d,i}}(t), \mathbf{y_i}(t)\big)$, which is later applied as the *feature* of the dataset. The DAQ then *labels* the sequence with the sampled ground truth condition instance $c_{\epsilon,i}$, thus creating a supervised data pair $\mathcal{D}_i = \{\boldsymbol{\mathcal{X}}_i(t), c_{\epsilon,i}\}$. The antagonist follows the same procedure enumerating every condition instance $c_{\epsilon,i} \in \mathbb{C}_\epsilon$ and formulates a dataset $\mathcal{D} = \big\{\{\mathcal{D}_i\}_{i=1}^{k}\big\}$ where $k$ represents the number of synthetic runtimes. Aside from the CWRU dataset [20], the Machinery Fault Simulator [18], an influential commercial product for rotordynamic FDD studies [21], adopts the identical M-CS practice to install modular faulty condition instances on rotordynamic plants for a broader $\mathbb{C}_\epsilon$, made up of an eccentric mass, a cocked rotor, a centrally bent shaft, and various faulty bearings. The same M-CS pipeline are universally adopted in previous rotordynamic CS practices [13–17,19].

## III. Robotic Condition Synthesis - Method

This section first provides a model-based perspective of condition synthesis. Further, a novel Robotic Condition Synthesis pipeline is proposed.

### A. Objective of Condition Synthesis

Condition synthesis is the data source supplier for investigating new FDD techniques. Understanding the demand of FDD is critical to analyze the ideal method for condition synthesis. Consider a generic rotordynamic plant [22]:

$$\mathbf{M}\ddot{\mathbf{q}} + \mathbf{B}\dot{\mathbf{q}} + \mathbf{C} + \mathbf{G} = \mathbf{Q} \tag{1}$$

where $\mathbf{M},\mathbf{B},\mathbf{C},\mathbf{G}$ are the plant's physical parameters, i.e., inertial, damping, Coriolis, and gravitational matrices; $\mathbf{q}$ is the generalized displacement vector; and $\mathbf{Q}$ is the generalized inputs considering components from external sources, i.e., the operator's input $\mathbf{Q_d}$ for normal operation, and the perturbation $\mathbf{Q}_\epsilon$:

$$\mathbf{Q_d} = \mathbf{M}\ddot{\mathbf{q}} + \mathbf{B}\dot{\mathbf{q}} + \mathbf{C} + \mathbf{G} + \mathbf{Q}_\epsilon \tag{2}$$

Without loss of generality, through a linear state observer with observation matrices $\mathbf{C_o}$ and $\mathbf{D_o}$, the output of the system is:

$$\mathbf{y} = \mathbf{C_o q} + \mathbf{D_o Q_d} \tag{3}$$

It is critical to realize that a shared core of most condition synthesis practices is to perturb the dynamics of the baseline rotor plant, i.e., modulating $\mathbf{Q}_\epsilon$ with different *modalities* at various *severity levels*. The M-CS practices achieve it by enumerating a predefined set of healthy/faulty conditions. During M-CS, the rotordynamic plant is perturbed by the sampled condition instance $c_{\epsilon,i}$:

$$\mathbf{Q}_{\epsilon,i}(t) = g_{c_{\epsilon,i}}\big(\mathbf{q}(t), \dot{\mathbf{q}}(t), ...\big), \quad \text{s.t.} \quad c_{\epsilon,i} \in \mathbb{C}_\epsilon \tag{4}$$

where $g_{c_{\epsilon,i}}(\cdot)$ denotes a generic expression that reflects the perturbation of the specific condition instance $c_{\epsilon,i}$. While Eqn.4 is an ideal generalization of condition synthesis, it is rare to find either the high-fidelity analytical expression $g_{c_{\epsilon,i}}(\cdot)$, or its required inputs readily available [23] in practice. When more complex factors are considered, e.g., process noise and modality superposition, the attempts to measure or feed-forwardly roll out $\mathbf{Q}_{\epsilon,i}(t)$ as labels of the dataset are futile. Consequently, existing M-CS practice records each sampled condition instance as the label instead, i.e., $\mathcal{D}_i = \{\boldsymbol{\mathcal{X}}_i(t), c_{\epsilon,i}\}$. The M-CS generated datasets are then used to train FDD algorithms to classify the condition instances based on the time-series features.

The existing M-CS approaches suffer from several drawbacks. First, the progression of faults, such as the growth of a seeded hole that amplifies vibration, often contains more informative data than steady-state signals [16]. However, the perturbation in Eqn.4 cannot be actively modulated, as $\mathbf{Q}_\epsilon(t)$ is not controlled during the M-CS process, resulting in the inability to synthesize fault progressions. Second, since $\mathbf{Q}_\epsilon(t)$ is not observable during M-CS, the only useful label for the time-series data feature is the condition instance installed to generate the sequence. This *one-label-per-sequence* annotation, unless aided by self-supervision or auto-regressive techniques, limits the predictive capacity of FDD algorithms to hindsight diagnoses [6]. Third, the condition space $\mathbb{C}$ is practically infinitely dimensional and continuous, with a simple plant facing infinite variations of faulty conditions, each with a continuous severity level. In contrast, the predefined condition set in M-CS, $\mathbb{C}_\epsilon$, is often sparse, discrete, and small, compromising the efficiency of manual enumeration and raising significant coverage concerns [6,24,25]. Finally, the human involvement during the fault-seeding, condition-sampling, and instance-installation stages of the M-CS process in Fig.1 leads to further reduced efficiency and synthesis repeatability. Considering the large amount of data required to meet the demands of FDD studies, M-CS is not an ideal solution. These suboptimal properties motivate exploring a solution that utilizes robots to replace humans in the condition synthesis loop.

### B. Robotic Condition Synthesis Method

In order to efficiently synthesize conditions on rotordynamic plants using robots, we formulate the R-CS process as a robotic force control problem. As indicated by Eqn.2 and Eqn.3, condition synthesis is essentially the modulation of rotordynamics through perturbations $\mathbf{Q}_\epsilon(t)$. These perturbed dynamics result in a mismatch between the input $\mathbf{Q_d}(t)$ and observations $\mathbf{y}(t)$ compared to

healthy dynamics, which FDD algorithms aim to exploit to estimate the condition correctly. The challenge with manual Condition Synthesis is that $\mathbf{Q}_\epsilon(t)$ is inherently not controllable or observable through the installation of faulty components. However, active force control and observation of $\mathbf{Q}_\epsilon(t)$ are technically feasible with appropriate robot and control policy design. The generalized perturbation encompasses four attributes: axial and lateral forces $(P_\epsilon, V_\epsilon)$ and bending moment and torque $(M_\epsilon, \tau_\epsilon)$. To facilitate a better abstraction, we propose a quantitative Condition State Space (CSS), where $\mathbf{Q}_\epsilon \in \mathbb{R}^4$ is the condition state variable, as depicted in Fig.1.

This leads to two subsequent challenges: first, how to design the control policies of the condition state variable $\mathbf{Q}_\epsilon$ to recover healthy/faulty conditions in the original condition space with high fidelity? Second, how to instrument the robot to carry out predefined policies? While this study focuses on the latter challenge, we summarize the essential features of the R-CS policies. From past literature, we conclude that different healthy/faulty conditions on rotordynamic plants exhibit two dominating modalities: imposing mechanical impedance dynamics and modulating self-excited/forced vibration at different severity levels. To synthesize these characteristics with robots, we propose the robot's *control policy* corresponds to the *modality* of healthy/faulty conditions, and the *control parameters* corresponds to the *severity* of the behavior. Accordingly, we propose two control policies: virtual impedance control $(\pi_{\text{VIC}})$ and active vibration injection $(\pi_{\text{AVI}})$ to mimic the impedance and vibrational behaviors, respectively. Their control parameters are denoted as $\phi_{\text{VIC}}$ and $\phi_{\text{AVI}}$. The VIC synthesis is expressed as:

$$\begin{aligned}\mathbf{Q}_\epsilon(t) &= \pi_{\text{VIC}}(\phi_{\text{VIC}}) \\ &= -\mathbf{M}\ddot{\mathbf{q}}_\mathbf{d} - \mathbf{B}\dot{\mathbf{q}} - \mathbf{C} - \mathbf{G} + \mathbf{B}_\epsilon(\dot{\mathbf{q}} - \dot{\mathbf{q}}_\mathbf{d}) + \mathbf{K}_\epsilon(\mathbf{q} - \mathbf{q}_\mathbf{d})\end{aligned} \tag{5}$$

where $\mathbf{B}_\epsilon, \mathbf{K}_\epsilon \in \phi_{\text{VIC}}$ are the desired virtual damping and stiffness matrices to imitate a target condition instance; $\mathbf{q}_\mathbf{d} \in \phi_{\text{VIC}}$ is the desired generalized displacement. The AVI policy is designed as:

$$\mathbf{Q}_\epsilon(t) = \pi_{\text{AVI}}(\phi_{\text{AVI}}) = \mathbf{Q}_{\epsilon,\mathbf{b}} \cos(\omega_\epsilon t) + \mathbf{Q}_{\epsilon,\mathbf{a}} \tag{6}$$

where $\mathbf{Q}_{\epsilon,\mathbf{b}}, \mathbf{Q}_{\epsilon,\mathbf{a}}, \omega_\epsilon \in \phi_{\text{AVI}}$ denotes the vibration amplitudes, offsets, and frequency for the robot to inject into the rotordynamic plant, the VIC regulates the plant dynamic to mimic the impedance terms exerted by certain healthy/faulty conditions. The AVI policy actively induces forced vibration to the rotordynamic plant to imitate the vibrational components - up to $4\times$ plant's rotational frequency $\Omega_s$ [16] - that manifest in common healthy/faulty conditions of rotordynamic plants. A full derivation of the control policies is important but goes beyond the scope of this study. Interested readers are pointed to [16,26,27] to model the common rotordynamic faults, including rotor unbalance, drive-train misalignment, cracks, rub-impact, and bearing faults, as impedance or vibratory inputs.

The R-CS pipeline in Fig.1 is principally more advantageous than M-CS. First, for every synthetic runtime $i$, the controllable $\mathbf{Q}_{\epsilon,\mathbf{i}}(t)$ allows real-time modulation of the plant dynamic and an augmented *one-label-per-time-step* annotation, i.e., $\mathcal{D}_i = \{\boldsymbol{\mathcal{X}}_i(t), \mathbf{Q}_{\epsilon,i}(t), \phi_{\text{VIC},i}(t), \phi_{\text{AVI},i}(t)\}$. The former enables state transitions during the runtime, and the latter grants the generated dataset real-time predictive capacities to future FDD algorithm studies. Furthermore, the abstracted policies significantly streamline the sampling process. Instead of selecting individual condition instances in the *condition space*, the robotic antagonist can programmatically traverse the *policy subspaces* with various policy parameters to recover an extensive scope in the condition state space and, in turn, the original condition space, as depicted by Fig.1. Importantly, the core statement is to acknowledge the two control policies as the primary factor in deriving the contact model and the functional requirements of the R-CS instrument.

## IV. Robot Condition Synthesis - Instrument

### A. Manipulation Task and Contact Model

The objective of the R-CS robot is to deliver $\mathbf{Q}_\epsilon(t)$ to an arbitrary location along a rotor shaft according to the VIC or AVI policy. In this study, the robot's scope is condensed from delivering the generalized perturbation $\mathbf{Q}_\epsilon(t)$ to the lateral load $V_\epsilon(t)$ as an example of all four elements in the generalized perturbation.

The lateral-direction R-CS is an impedance-control problem for the VIC policy and an explicit force-control one for the AVI policy. To develop a desirable control system performance, it is critical to model the contact dynamics between the end-of-arm-tool(EoAT) and the rotor shaft. A world is initialized with a rotordynamic plant and a robot manipulator in Fig.2. The rotordynamic plant consists of a vanilla rotor shaft (of length $L_s$ and radius $r_s$) driven by a motor and is supported by bearings on both ends. The rotor plant's coordinate frame $S_{xyz}$, with unit vectors $< \mathbf{i}^\mathbf{S}, \mathbf{j}^\mathbf{S}, \mathbf{k}^\mathbf{S} >$, is anchored at the near-motor bearing. The following adopts "*lateral*" to describe the $\mathbf{i}^\mathbf{S}$ direction, and "*axial*" the $\mathbf{k}^\mathbf{S}$ direction. The intrinsic lateral dynamics of the shaft are representable by a lumped mass-spring-damper (MSD) model with effective inertial $m_s$, damping $b_s$, and stiffness $k_s$, as visualized on the top-right of Fig.2. Notably, these parameters depend on the distance from the near-motor support, $z_s$ [28]. The lateral MSD dynamic is:

$$G_S(s, z_s) = \frac{\delta x_s(s, z_s)}{V_\epsilon(s, z_s)} = \frac{1}{m_s(z_s)s^2 + b_s(z_s)s + k_s(z_s)} \tag{7}$$

where $\delta x_s$ is the lateral displacement of the shaft and $s$ is the Laplace-variable. The coordinate frame for the robot's base and EoAT (of mass $m_e$) is denoted as $R_{xyz}$ and $E_{xyz}$, respectively. Without loss of generality, consider a fully actuated 6 degree-of-freedom robot in SE(3) with joint-space displacement vector $\mathbf{q_r} \in \mathbb{R}^6$ and task-space displacement $\mathbf{x_E} \in \mathbb{R}^6$. Assuming an invertible manipulator Jacobian of the robot $\mathbf{J_e}^T \in \mathbb{R}^{6\times6}$, the task-space force output of the manipulator $\mathbf{F_E} \in \mathbb{R}^6$ is:

$$\mathbf{F_E}(s) = (\mathbf{J_e}^T)^{-1}\boldsymbol{\tau}(s) = (\mathbf{J_e}^T)^{-1}\mathbf{u}(s)\frac{s}{s+a} \tag{8}$$

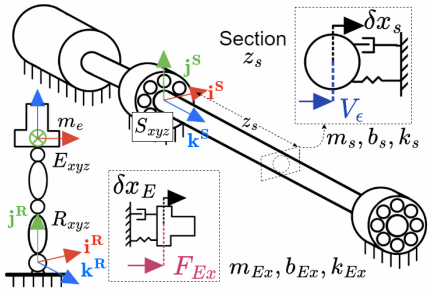


Fig. 2. The initialized world includes the plant and the CaMAR. The boxed schemes are their respective lumped models.

where $\boldsymbol{\tau}, \mathbf{u} \in \mathbb{R}^6$ is the joint actuation and control effort vector, respectively; $a$ is a scalar to represent the first-order low-pass dynamic of each actuator, assuming identical actuators on all joints. The transfer function from individual joint actuator inputs to the lateral ($\mathbf{i^S}$) component of task-space force output $F_{Ex}$ is:

$$\mathbf{G_u}(s) = \left[\frac{F_{Ex}(s)}{u_1(s)}, ..., \frac{F_{Ex}(s)}{u_6(s)}\right]^T = (\mathbf{J_e}^T)^{-1}\mathbf{i^S}\frac{s}{s+a} \tag{9}$$

The full unloaded task-space dynamic of the robot is:

$$\mathbf{F_E}(t) = \boldsymbol{\Lambda}(\mathbf{q_r})\ddot{\mathbf{x}}_\mathbf{E} + \boldsymbol{\mu}(\mathbf{x_E}, \dot{\mathbf{x}}_\mathbf{E}) + \boldsymbol{\gamma}(\mathbf{q_r}) + \boldsymbol{\eta}(\mathbf{q_r}, \dot{\mathbf{q}}_\mathbf{r}) \tag{10}$$

where $\boldsymbol{\Lambda}$ is the task-space inertial matrix; $\boldsymbol{\mu}, \boldsymbol{\gamma}, \boldsymbol{\eta}$ are the Coriolis and centrifugal term, the gravitation, and other nonlinear terms. Unfortunately, the manipulator dynamics in Eqn.10 is highly nonlinear. At present, assuming the task-space manipulator dynamic along $\mathbf{i^S}$ direction can be lumped to an MSD model in Fig.2 with parameters $m_{Ex}, b_{Ex}, k_{Ex}$, the simplified dynamics of the EoAT is thus:

$$G_E(s) = \frac{\delta x_E(s)}{F_{Ex}(s)} = \frac{1}{m_{Ex}s^2 + b_{Ex}s + k_{Ex}} \tag{11}$$

This simplification is eventually realized via a Cartesian-space kinematics and a multi-actuation dynamics, as we will discuss in detail during the robot design in Sec.IV-C. After contact is formed between the EoAT and the shaft, the dynamics is coupled. The top right schematic of Fig.3 represents a compliant contact interface with stiffness $k_i$ and damping $b_i$:

$$H_{soft}(s, z_s) = \frac{V_\epsilon(s, z_s)}{F_{Ex}(s)} = \frac{H_s H_i}{H_s H_i + H_{Ex}(H_s + H_i)} \tag{12}$$

where:

$$\begin{aligned} H_{Ex} &= m_{Ex}s^2 + b_{Ex}s + k_{Ex} \\ H_s &= m_s(z_s)s^2 + b_s(z_s)s + k_s(z_s) \\ H_i &= b_i s + k_i \end{aligned} \tag{13}$$

For a rigid contact, $k_i \to \infty$ and $b_i s \to 0$:

$$H_{rigid}(s, z_s) = \frac{V_\epsilon(s, z_s)}{F_{Ex}(s)} = \frac{H_s}{H_s + H_{Ex}} \tag{14}$$

The force-loop transfer function is defined as:

$$\mathbf{G_V}(s, z_s) = \left[\frac{V_\epsilon(s, z_s)}{u_1(s)}, ..., \frac{V_\epsilon(s, z_s)}{u_6(s)}\right]^T = \mathbf{G_u}(s) \cdot H_{contact}(s, z_s) \tag{15}$$

where $H_{contact} \in \{H_{soft}, H_{rigid}\}$ is the selected contact interface model. The above derivation helps us identify the robot's critical functional requirements for R-CS.

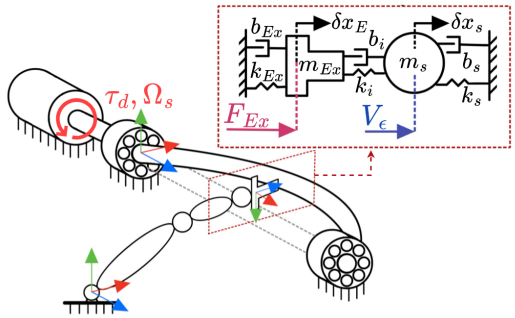


Fig. 3. Illustration of the contact dynamics between the robot and the rotor shaft.

### B. Robot's Functional Requirement

The manipulation task and contact model result in five functional requirements for the robot: (a) Workspace: The robot's end-of-arm tool must be able to reach the maximum lateral deflection of the shaft, $\max(\delta x_s)$, and any axial location on the shaft $[0, L_s]$. (b) Force-loop bandwidth: The force-loop bandwidth $f_F$ describes the bandwidth of system Eqn.15. It has two demands. First, the AVI policy aims to inject vibration frequency up to four $4\times$ rotational frequency $\Omega_s$ into the rotordynamic plant. Second, to achieve impedance control in the VIC policy, position-based force control is a well-suited method, with an inner position loop nested by an outer force control loop [29]. Thus, a high force-loop bandwidth is crucial for both policies. The requirement $f_F \geq 4\Omega_s$ finds a reasonable balance between R-CS performance and instrumentation difficulty. (c) Repeatability: Force output is sensitive to positional displacement, and the R-CS tasks are especially contact-rich, so fine repeatabilities along critical directions are essential. Simultaneously, the VIC and AVI policies require high EoAT velocity. Overloading the robot's computational resources, such as the FPGA in its host computer, with unnecessarily fine positional repeatability can impair its performance. Thus, we propose lateral precision of $O(10\mu m)$ as a balance between measurement accuracy and EoAT velocity. The axial repeatability requirement is $O(100\mu m)$, which benchmarks common lab-grade articulated robots. (d) Payload: The robot's main payload requirement is to deform the rotor shaft along the lateral direction during the VIC operation. A simplified relationship between a static shaft's deflection and the lateral force input is modeled in Eqn.7. The detailed model combining the Euler-Bernoulli beam theory with rotordynamics for static and rotating shafts is well-studied [30]. (e) Nonlinearity: the R-CS policies aim to deliver clean but oscillatory force trajectories. Mechanical nonlinearities, such as backlash and friction, create a force deadband and impair the trajectory, so the robot requires its design to minimize physical nonlinearity.

These R-CS-induced functional requirements are beyond the capacity of lab-grade articulated manipulators. The ideal robot requires a high force bandwidth, high repeatability, and minimal backlash. Although commercial general-purpose lab-grade manipulators [7–9] offer extensive workspaces and high dexterities, they are unsuitable for high task-space force-bandwidth tasks because of their extended links, and large reflected joint-actuator inertia [31]. Additionally, the backlash for these articulated robots is notably on $O(1)mm$ scale, tolerable for common uni-directionally loaded tasks but not for oscillatory force trajectories required by R-CS. The repeatabilities of these manipulators are mostly $\pm 0.1mm$, and do not suffice the R-CS functional requirement. Although there have been a few high-bandwidth manipulators proposed in literature[32,33], they are intended for millimeter-scale workspace and low-payload tasks and are difficult to generalize to larger length scales. Sharon et al. [34] and Lopes et al. [29] each propose a macro-micro robot that stacks two manipulators to leverage the macro manipulator's extensive workspace and the micro manipulator's high bandwidth. This is similar to the multi-actuation concept we adopt in the following. However, their complex kinodynamics, 10+ degree-of-freedom, and budget overheads make them not easily generalizable to the FDD community.

The vacancy of a suitable manipulator for R−CS consequently inspires the development of the novel robot - the CaMAR.

### C. Robot Design and Development

The gist of the CaMAR's design is to satisfy the proposed functional requirements and simultaneously minimize the complexity of carrying out the VIC and AVI policies. The Cartesian Multi-Actuation Robot achieves this objective with two leverages. First, by aligning the robot's base frame with the world frame, the robot's Cartesian structure can significantly reduce the complexity of the manipulation task by removing trigonometry in the rotational element of the manipulator Jacobian matrix, creating a linear mapping between its joint and task spaces. Furthermore, an important assumption to linearize the EoAT's dynamics from Eqn.10 to Eqn.11 was proposed in Sec.IV-A, which is untenable for revolute articulated robots. However, the CaMAR's Cartesian structure minimizes the Coriolis and centrifugal terms and structurally dissipates the gravitational loads in Eqn.10, thus realizing this assumption. Second, the CaMAR adopts a multi-actuation structure to enhance the system-level performance by complementing the strengths of individual joints. The robot's multi-actuation structure combines coarse-repeatability large-range-of-motion(ROM) joints with *redundant* fine-repeatability small-ROM high-bandwidth joints to enhance overall performance at the EoAT.

Without loss of generality, a 3-prismatic joint CaMAR is designed and depicted in Fig.4. The first joint ($J1$) provides the $O(1m)$ axial workspace in the world frame. Since the critical direction for the CaMAR's operation is along the lateral ($\mathbf{i}^{\mathbf{S}}$) axis, multi-actuated redundant joints ($J2, J3$) are proposed to cooperatively achieve $O(10mm)$ length-scale ROM and $O(10\mu m)$ repeatability. Effective methods based on dielectric/piezoelectric actuation, previously used in nano-positioning systems [35,36], are not the best option for this design due to their limited ROMs. Instead, a heterogeneous set of actuation methods is designed for CaMAR: $J1$ is equipped with a stepper-actuated linear rail to provide high positional resolution, zero backlash, and locking capacity. $J2$ uses a preloaded lead-screw mechanism to offer mechanical locking capacity, zero backlash, and high payload. The locking capabilities of $J1$ and $J2$ decouple their dynamic effects from $J3$, which provides the final force trajectory to the rotor shaft. This unique hardware design and actuation combination reduce the complexity of manipulation by collapsing the controller input vectors in Eqn.8 and 9 to a single dimension. As suggested in [31], reducing the reflective inertia of joints and links is an effective way to achieve high contact force bandwidth. The

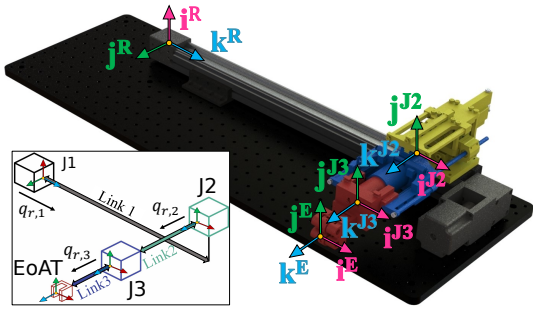


Fig. 4. A 3-prismatic joint CaMAR. CaMAR's design method is generalizable to high-degree-of-freedom versions.

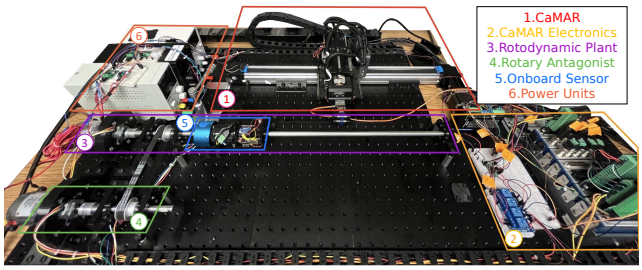


Fig. 5. Overview of the instrumented R−CS platform with the CaMAR.

CaMAR exploits this principle by adopting a voice-coil-actuator (VCA) in $J3$. Its direct-drive nature and decoupled multi-actuation dynamic collectively help reduce the reflective inertia in the contact model (Eqn.15) to $m_{Ex} \rightarrow m_e + m_v$ - where $m_e, m_v$ is the mass of EoAT and the VCA's solenoid, respectively - as opposed to the full task-space inertia in regular articulated robots. Thus, a high force-loop bandwidth at the EoAT is expected.

### D. Instrumentation

The rotordynamic plant's specifications are presented for reproducibility. The rotor shaft is $750mm$ in length and $10mm$ in radius. The axial range subject to the condition synthesis is $500mm$, i.e., $L_s = 500mm$, supported by self-aligning bearings on both ends. The rotational speed of the plant is between 200-1000rpm.

The CaMAR instrumentation is summarized as follows. $J1$ consists of a $500mm$-stroke linear rail driven by a 2.8A NEMA23 stepper motor. $J2$ is powered by a 12V DC motor. The joint provides a $50mm$ stroke and 200N maximum payload. $J1$ and $J2$ support 115N and 102N holding forces, respectively. $J3$ consists of a 43V DC VCA. The joint provides a $25mm$ stroke, 44N maximum payload and 12N continuous load. The payload of the overall manipulator can theoretically induce a static lateral reflection $\max(\delta x) = 5.8mm$ at the axial center of the rotor shaft, orders of magnitude larger than the allowable deflection in most industrial rotary machines. The structural components in $J1$ and $J2$ are CNC-routed with 6061 Aluminum to achieve high rigidity and low inertia. Modular EoATs are installed on $J3$. They are 3d-printed in Nylon-infilled carbon fiber to ensure geometrical precision and rigidity and simultaneously minimize $m_e$ to improve the manipulator's dynamic performance further. The CaMAR adopts a hierarchical software architecture. The host machine in LabVIEW serializes a NI-cRIO-9074 for the CaMAR and a NI-cRIO-9073 for the rotordynamic plant. The primary control logic is implemented using LabVIEW FPGA on both cRIOs with 40MHz clock rates. A full setup is displayed in Fig.5.

## V. Experiment and Validation

We carry out three experiments to demonstrate preliminary R−CS results and validate the CaMAR in the R−CS pipeline.

### A. Standard Performance Test

In the first set of experiments, we illustrate that the two critical functional requirements are accomplished by the unique robot design: (a) Bandwidth: Open-loop positional bandwidth $f_P$, for Eqn.11, and force bandwidth $f_F$ are empirically determined. For both experiments, $J1$ and $J2$ are locked, and the inputs are PWM control effort to the VCA. The output is the EoAT displacement $\delta x_s$ and injected load $V_\epsilon$, respectively. To obtain the latter, the

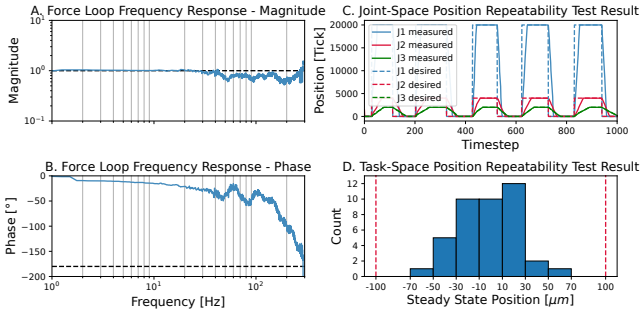


Fig. 6. Standard performance test result of the CaMAR.

EoAT is grounded by a fixture, such that the contact model in Eqn.14 is assumed rigid. The CaMAR achieves $f_P = 12$Hz, much higher than the $2-5$Hz range of lab-grade articulated robots [7–9]. The force loop bode plot is demonstrated in Fig.6-A and B. Strictly following the definition of the mechanical bandwidth, i.e., -3dB decay from DC gain, the force-loop bandwidth $f_F \approx 50$Hz, is slightly deficient in satisfying the functional requirement $f_F \geq 4\Omega_s$, where $\max(\Omega_s) = 1000$rpm$\approx 16.67$Hz as specified previously. However, the robot's gain does not decay beyond 50Hz but stays consistently between half and unit gain up to 200Hz. An over-60° phase margin is maintained in that frequency range. This scenario is different from what is described by the mechanical bandwidth. In fact, the above open-loop result indicates that a closed-loop force controller can be effortlessly designed for 200Hz condition synthesis operation, which is an exceedingly satisfactory performance for the CaMAR's functional requirement. (b) Repeatability: All joints are fully extended and retracted, and the steady-state positions are measured in the joint space by the embedded linear encoders and in the task space by a $0.001mm$-resolution dial indicator. Fig.6-B demonstrates the joint-space position tracking performance of all three joints. Along the multi-actuation (lateral) direction, both joints settle within $\pm 30\mu m$ the commanded positions, and the collective repeatability is upper-bounded by $\pm 60\mu m$. Fig.6-D demonstrates the task-space repeatability result along the lateral direction for over 40 reciprocals. The majority of steady-state responses fall within the $\pm 50\mu m$ range, with a handful of extreme cases within $\pm 70\mu m$ range. It is safe to conclude that the CaMAR significantly outperforms the $\pm 100\mu$m standard of most accessible robots.

### B. Active Vibration Injection Validation

In this experiment, a closed-loop `AVI` policy is carried out to the rotordynamic plant. The `AVI` trajectory is injected to the $z_s = \frac{23}{24} L_s$ location of a static shaft. Following Eqn.6, the `AVI` parameters are $V_{\epsilon,a} = 15$N, $V_{\epsilon,b} = 5$N. The injected frequency $\omega_\epsilon$ sweeps a range of $0.1-45$Hz, as indicated by the dotted reference in Fig.7. A Short-time Fourier transform (STFT) is conducted on onboard-sensor signals that are used to capture the features $\mathbf{y_i}(t)$. Both examples in Fig.7 show visually amplified frequency components that follow the injected frequency trajectory. This

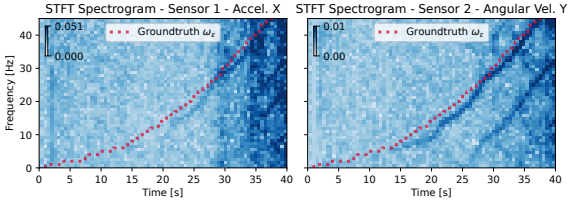


Fig. 7. The `AVI` experiment result.

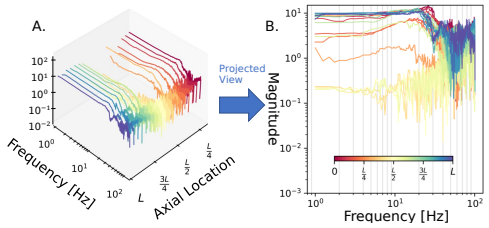


Fig. 8. Lateral dynamics' frequency response along the axial direction. Fig.B is a projection of Fig.A on the 'Axial Location' plane for a better illustration.

experiment illustrates the CaMAR's capacity to modulate the original plant dynamics with controlled time-varying vibration. This is an important distinction between the state-transitional `R-CS` and state-of-the-art `M-CS`. Furthermore, the onboard sensors can capture distinctive signals that are interpretable even for an untrained human, indicating a huge potential of the `R-CS` method for learning-based `FDD`.

### C. Lateral Dynamics Identification

This experiment identifies the lateral dynamics of the rotor plant along its axial direction. While the above `AVI` experiment demonstrates a successful open-loop force control, it is worth noting that the `AVI` experiment is conducted at a particular location of the rotor shaft. As indicated by Eqn.7, the lateral dynamics of the shaft are dependent on its axial location, which affects the coupled contact model in Eqn.15. Thus, it is crucial to empirically evaluate these complex axial-location-dependent lateral dynamics in order to develop effective control systems for both `R-CS` policies in closed loops. The CaMAR enables a three-dimensional system identification of the lateral dynamics at 19 axial locations $z_s \in [\frac{2}{11}L, L]$. As shown in Fig.8, the results indicate that it becomes increasingly challenging to generate large lateral loads on the shaft as the CaMAR approaches the center of the shaft, in accordance with the fact that the mechanical impedance of the shaft is lowest at the axial center and highest at the supports. The lateral dynamics within $\frac{L}{4}$ from the supports are consistent among each other, with the first resonant frequency around 20-25Hz and a second resonant at approximately 40Hz. This experiment yields two key insights: first, it proves the practical utility of the CaMAR in an `R-CS` task. Second, the identified system dynamics are the fundamental stepping stones to achieving high-performance `R-CS` policies, which will be the subject of a future comprehensive study.

## VI. Conclusion and Future Work

We propose a novel method, Robotic Condition Synthesis, to generate high-quality data for fault detection and diagnosis development efficiently. Our method transforms traditional condition synthesis from manual to an efficient robotic force control problem. Further, we propose a novel Cartesian Multi-Actuation Robot as an effective `R-CS` instrument. We empirically validate that the hardware design of CaMAR intrinsically yields dynamical superiority over lab-grade manipulators. We further illustrate a successful `AVI` injection that embeds real-time condition state transitions. Lastly, we conduct a three-dimensional lateral dynamic identification of the rotor plant, which lays a fundamental building block for in-depth developments of `R-CS` control policies in the upcoming studies.

## References


[1] J. Zhang, W. Ma, J. Lin, L. Ma, and X. Jia, "Fault diagnosis approach for rotating machinery based on dynamic model and computational intelligence," 2015.

[2] A. Heng, S. Zhang, A. C. C. Tan, and J. Mathew, "Rotating machinery prognostics: State of the art, challenges and opportunities," *Mech. Syst. Signal Process.*, vol. 23, pp. 724–739, Apr. 2009.

[3] V. Chandola, A. Banerjee, and V. Kumar, "Anomaly detection: A survey," *ACM Comput. Surv.*, vol. 41, pp. 1–58, July 2009.

[4] Y. F. Yeung, A. Alshehri, L. Wampler, M. Furokawa, T. Hirano, and K. Youcef-toumi, "A General-Purpose anomalous scenario synthesizer for rotary equipment," in *IEEE International Conference on Robotics and Automation*, 2021.

[5] T. Hu, T. Tang, R. Lin, M. Chen, S. Han, and J. Wu, "A simple data augmentation algorithm and a self-adaptive convolutional architecture for few-shot fault diagnosis under different working conditions," *Measurement*, vol. 156, p. 107539, May 2020.

[6] Y. F. Yeung, A. Alshehri, A. Paul-Ajuwape, F. Tahiry, M. Furokawa, T. Hirano, and K. Youcef-toumi, "RoSA:A mechatronically synthesized dataset for rotodynamic system anomaly detection," in *IEEE/RSJ International Conference on Intelligent Robots and Systems (IROS)*, 2022.

[7] "Dobot magician." https://www.dobot.us/. Accessed: 2022-8-5.

[8] "LBR iiwa." https : / / www . kuka . com / en - us / products / robotics - systems/industrial-robots/lbr-iiwa. Accessed: 2022-8-5.

[9] "The UR5e - a flexible collaborative robot arm." https://www.universal-robots.com/products/ur5-robot/. Accessed: 2022-8-5.

[10] Y. F. Yeung, A. AlShehri, L. Wampler, T. Hirano, M. Furokawa, and K. Youcef-Toumi, "Modular, general purpose, automated, anomalous data synthesizers for rotary plants," May 2022.

[11] S. Poll, A. Patterson-Hine, J. Camisa, D. Garcia, D. Hall, C. Lee, O. J. Mengshoel, C. Neukom, D. Nishikawa, J. Ossenfort, and Others, "Advanced diagnostics and prognostics testbed," in *Proceedings of the 18th International Workshop on Principles of Diagnosis (DX-07)*, pp. 178–185, 2007.

[12] S. Yin and X. Zhu, "Intelligent particle filter and its application to fault detection of nonlinear system," *IEEE Trans. Ind. Electron.*, vol. 62, pp. 3852–3861, June 2015.

[13] O. Janssens, V. Slavkovikj, B. Vervisch, K. Stockman, M. Loccufier, S. Verstockt, R. Van de Walle, and S. Van Hoecke, "Convolutional neural network based fault detection for rotating machinery," *J. Sound Vib.*, vol. 377, pp. 331–345, Sept. 2016.

[14] Y. Gao, X. Liu, and J. Xiang, "FEM Simulation-Based generative adversarial networks to detect bearing faults," *IEEE Trans. Ind. Inf.*, vol. 16, pp. 4961–4971, July 2020.

[15] T. Ince, S. Kiranyaz, L. Eren, M. Askar, and M. Gabbouj, "Real-Time motor fault detection by 1-D convolutional neural networks," *IEEE Trans. Ind. Electron.*, vol. 63, pp. 7067–7075, Nov. 2016.

[16] N. H. Chandra and A. S. Sekhar, "Fault detection in rotor bearing systems using time frequency techniques," *Mech. Syst. Signal Process.*, vol. 72-73, pp. 105–133, May 2016.

[17] F. M. L. Ribeiro, "Machinery fault database [online]." http : //www02.smt.ufrj.br/~offshore/mfs/. Accessed: 2022-4-29.

[18] SpectraQuest, Inc, "Machinery fault simulator." https://spectraquest.com/machinery-fault-simulator/. Accessed: 2022-4-12.

[19] S. P. Mogal and D. I. Lalwani, "Fault diagnosis of bent shaft in rotor bearing system," *J. Mech. Sci. Technol.*, vol. 31, no. 1, pp. 2–5, 2017.

[20] Case Western Reserve University Bearing Data Center, "CWRU bearing dataset." https://csegroups.case.edu/bearingdatacenter/home. Accessed: 2022-1-29.

[21] A. M. Mustafa and J. F. Nayfeh, "Experimental research on machinery fault simulator (MFS): A review," in *2020 Prognostics and Health Management Conference*, pp. 72–78, May 2020.

[22] G. Genta, *Dynamics of Rotating Systems*. Springer Science & Business Media, Apr. 2005.

[23] H. Huang, L. Yang, Y. Wang, X. Xu, and Y. Lu, "Digital twin-driven online anomaly detection for an automation system based on edge intelligence," *Journal of Manufacturing Systems*, vol. 59, pp. 138–150, Apr. 2021.

[24] P. Gangsar and R. Tiwari, "Comparative investigation of vibration and current monitoring for prediction of mechanical and electrical faults in induction motor based on multiclass-support vector machine algorithms," *Mech. Syst. Signal Process.*, vol. 94, pp. 464–481, 2017.

[25] G. Bode, S. Thul, M. Baranski, and D. Müller, "Real-world application of machine-learning-based fault detection trained with experimental data," *Energy*, vol. 198, p. 117323, May 2020.

[26] W. J. Chen, *Practical rotordynamics and fluid film bearing design*. Eigen Technologies, Incorporated, 2015.

[27] P. Gangsar and R. Tiwari, "Signal based condition monitoring techniques for fault detection and diagnosis of induction motors: A state-of-the-art review," *Mech. Syst. Signal Process.*, vol. 144, p. 106908, Oct. 2020.

[28] F. J. Rubio-Sierra, R. Vazquez, and R. W. Stark, "Transfer function analysis of the micro cantilever used in atomic force microscopy," *IEEE Trans. Nanotechnol.*, vol. 5, pp. 692–700, Nov. 2006.

[29] A. Lopes and F. Almeida, "A force–impedance controlled industrial robot using an active robotic auxiliary device," *Robot. Comput. Integr. Manuf.*, vol. 24, pp. 299–309, June 2008.

[30] C. Beards, *Structural Vibration: Analysis and Damping*. Elsevier, May 1996.

[31] P. M. Wensing, A. Wang, S. Seok, D. Otten, J. Lang, and S. Kim, "Proprioceptive actuator design in the MIT cheetah: Impact mitigation and high-bandwidth physical interaction for dynamic legged robots," *IEEE Trans. Rob.*, vol. 33, no. 3, pp. 509–522, 2017.

[32] H. McClintock, F. Z. Temel, N. Doshi, J.-S. Koh, and R. J. Wood, "The millidelta: A high-bandwidth, high-precision, millimeter-scale delta robot," *Sci Robot*, vol. 3, Jan. 2018.

[33] Maxon, "Pocket delta robot." https://www.maxongroup.com/maxon/view/application/Pocket-sized-Delta-robots. Accessed: 2022-8-8.

[34] A. Sharon, N. Hogan, and D. E. Hardt, "The macro/micro manipulator: An improved architecture for robot control," *Robot. Comput. Integr. Manuf.*, vol. 10, pp. 209–222, June 1993.

[35] F. Xia, C. Yang, Y. Wang, and K. Youcef-Toumi, "Bandwidth based repetitive controller design for a modular multi-actuated AFM scanner," in *2019 American Control Conference (ACC)*, pp. 3776–3781, July 2019.

[36] F. Xia, S. Truncale, Y. Wang, and K. Youcef-Toumi, "Design and control of a multi-actuated high-bandwidth and large-range scanner for atomic force microscopy," in *2018 Annual American Control Conference (ACC)*, pp. 4330–4335, June 2018.